The Astrophysical Journal, 833:228 (12pp), 2016 December 20 doi:10.3847/1538-4357/833/2/228

BICEP2/*KECK ARRAY* VIII: MEASUREMENT OF GRAVITATIONAL LENSING FROM LARGE-SCALE *B*-MODE POLARIZATION

P. A. R. Ade[1], Z. Ahmed[2,3], R. W. Aikin[4], K. D. Alexander[5], D. Barkats[5], S. J. Benton[6], C. A. Bischoff[5], J. J. Bock[7,8], R. Bowens-Rubin[5], J. A. Brevik[7], I. Buder[5], E. Bullock[9], V. Buza[5,10], J. Connors[5], B. P. Crill[8], L. Duband[11], C. Dvorkin[10], J. P. Filippini[7,12], S. Fliescher[9], J. Grayson[2], M. Halpern[13], S. Harrison[5], S. R. Hildebrandt[7,8], G. C. Hilton[14], H. Hui[7], K. D. Irwin[2,3], J. Kang[2,3], K. S. Karkare[5], E. Karpel[2], J. P. Kaufman[15], B. G. Keating[15], S. Kefeli[7], S. A. Kernasovskiy[1], J. M. Kovac[5,10], C. L. Kuo[2,3], E. M. Leitch[16], M. Lueker[7], K. G. Megerian[8], T. Namikawa[2,3], C. B. Netterfield[6,17], H. T. Nguyen[8], R. O'Brient[7,8], R. W. Ogburn IV[2,3], A. Orlando[7], C. Pryke[9,18], S. Richter[5], R. Schwarz[18], C. D. Sheehy[16,18], Z. K. Staniszewski[7,8], B. Steinbach[7], R. V. Sudiwala[1], G. P. Teply[7,15], K. L. Thompson[2,3], J. E. Tolan[2], C. Tucker[1], A. D. Turner[8], A. G. Vieregg[5,16,19], A. C. Weber[8], D. V. Wiebe[13], J. Willmert[18], C. L. Wong[5,10], W. L. K. Wu[2,20], and K. W. Yoon[2]

(Keck Array and BICEP2 Collaborations)

[1] School of Physics and Astronomy, Cardiff University, Cardiff, CF24 3AA, UK
[2] Department of Physics, Stanford University, Stanford, CA 94305, USA; namikawa@slac.stanford.edu
[3] Kavli Institute for Particle Astrophysics and Cosmology, SLAC National Accelerator Laboratory, 2575 Sand Hill Road, Menlo Park, CA 94025, USA
[4] Department of Physics, California Institute of Technology, Pasadena, CA 91125, USA
[5] Harvard-Smithsonian Center for Astrophysics, 60 Garden Street MS 42, Cambridge, MA 02138, USA
[6] Department of Physics, University of Toronto, Toronto, Ontario, M5S 1A7, Canada
[7] Department of Physics, California Institute of Technology, Pasadena, CA 91125, USA
[8] Jet Propulsion Laboratory, Pasadena, CA 91109, USA
[9] Minnesota Institute for Astrophysics, University of Minnesota, Minneapolis, MN 55455, USA
[10] Department of Physics, Harvard University, Cambridge, MA 02138, USA
[11] Service des Basses Températures, Commissariat à l'Energie Atomique, F-38054 Grenoble, France
[12] Department of Physics, University of Illinois at Urbana-Champaign, Urbana, IL 61801, USA
[13] Department of Physics and Astronomy, University of British Columbia, Vancouver, British Columbia, V6T 1Z1, Canada
[14] National Institute of Standards and Technology, Boulder, CO 80305, USA
[15] Department of Physics, University of California at San Diego, La Jolla, CA 92093, USA
[16] Kavli Institute for Cosmological Physics, University of Chicago, Chicago, IL 60637, USA
[17] Canadian Institute for Advanced Research, Toronto, Ontario, M5G 1Z8, Canada
[18] School of Physics and Astronomy, University of Minnesota, Minneapolis, MN 55455, USA
[19] Department of Physics, Enrico Fermi Institute, University of Chicago, Chicago, IL 60637, USA
[20] Department of Physics, University of California, Berkeley, CA 94720, USA

Received 2016 June 3; revised 2016 August 17; accepted 2016 August 22; published 2016 December 19

ABSTRACT

We present measurements of polarization lensing using the 150 GHz maps, which include all data taken by the BICEP2 and *Keck Array* Cosmic Microwave Background polarization experiments up to and including the 2014 observing season (BK14). Despite their modest angular resolution ($\sim 0.^\circ 5$), the excellent sensitivity ($\sim 3\mu$K-arcmin) of these maps makes it possible to directly reconstruct the lensing potential using only information at larger angular scales ($\ell \leqslant 700$). From the auto-spectrum of the reconstructed potential, we measure an amplitude of the spectrum to be $A_{\rm L}^{\phi\phi} = 1.15 \pm 0.36$ (*Planck* ΛCDM prediction corresponds to $A_{\rm L}^{\phi\phi} = 1$) and reject the no-lensing hypothesis at 5.8σ, which is the highest significance achieved to date using an *EB* lensing estimator. Taking the cross-spectrum of the reconstructed potential with the *Planck* 2015 lensing map yields $A_{\rm L}^{\phi\phi} = 1.13 \pm 0.20$. These direct measurements of $A_{\rm L}^{\phi\phi}$ are consistent with the ΛCDM cosmology and with that derived from the previously reported BK14 *B*-mode auto-spectrum ($A_{\rm L}^{\rm BB} = 1.20 \pm 0.17$). We perform a series of null tests and consistency checks to show that these results are robust against systematics and are insensitive to analysis choices. These results unambiguously demonstrate that the *B* modes previously reported by BICEP/*Keck* at intermediate angular scales ($150 \lesssim \ell \lesssim 350$) are dominated by gravitational lensing. The good agreement between the lensing amplitudes obtained from the lensing reconstruction and *B*-mode spectrum starts to place constraints on any alternative cosmological sources of *B* modes at these angular scales.

Key words: cosmic background radiation – cosmology: observations – gravitational lensing: weak – polarization

1. INTRODUCTION

Cosmic Microwave Background (CMB) photons traveling from the surface of last scattering are lensed by the gravitational potential of the large-scale structure along the line of sight. This leads to spatial distortions of a few arcminutes in the temperature and polarization anisotropies. In particular, gravitational lensing converts some of the *E*-mode polarization into *B*-mode polarization (Zaldarriaga & Seljak 1998). Measurements of temperature and polarization with sufficient resolution and sensitivity can be used to reconstruct the intervening matter distribution, and, in the future, such bias-free measurements of large-scale structures will become some of the most powerful probes in cosmology (e.g., Hu 2002; Namikawa et al. 2010; Wu et al. 2014; Abazajian et al. 2015; Allison et al. 2015; Pan & Knox 2015). Lensing can also act as a noise source for primordial *B* modes,

which peak at degree scales (e.g., Kesden et al. 2002; Knox & Song 2002). With sufficient sensitivity, a reconstructed lensing potential can be used to predict the degree-scale lensing *B*-modes, enabling a deeper search for a primordial signal. If the tensor-to-scalar ratio r is below 0.01, such "delensing" procedures will become important in the search for inflationary *B*-modes (Kesden et al. 2002; Knox & Song 2002; Seljak & Hirata 2004; Smith et al. 2012). In the latest BICEP/*Keck* results, we already see a non-negligible lensing contribution at large angular scales ($\ell < 100$) (BICEP2/Keck *Array* Collaboration VI 2015).

Lensing reconstruction from high resolution CMB temperature maps has been performed using data from the Atacama Cosmology Telescope (ACT; Das et al. 2011, 2014), *Planck* (*Planck* Collaboration 2014a), and the South Pole Telescope (SPT; van Engelen et al. 2012; Story et al. 2015). More recently, reconstruction using polarization maps has also been demonstrated. Using polarization data, the estimated amplitude of the lensing potential power spectrum, $A_{\rm L}^{\phi\phi}$, from *Planck*2015, POLARBEAR, and SPTPOL are $A_{\rm L}^{\phi\phi} = 0.76 \pm 0.15$ (Planck Collaboration 2015), $A_{\rm L}^{\phi\phi} = 1.06 \pm 0.47$ (POLARBEAR Collaboration 2014b), and $A_{\rm L}^{\phi\phi} = 0.92 \pm 0.24$ (Story et al. 2015), respectively, where the errors denote the 1σ statistical uncertainties. The reconstructed lensing potential from the polarization maps can be used in cross-correlation with other lensing potential tracers, such as the cosmic-infrared background (CIB; Hanson et al. 2013; POLARBEAR Collaboration 2014a; van Engelen et al. 2015). These measurements all use the fact that a common lensing potential introduces statistical anisotropy into the observed CMB in the form of a correlation between the CMB polarization anisotropies and their spatial derivatives (Hu 2001; Hu & Okamoto 2002; Hirata & Seljak 2003a, 2003b). These experiments have high enough angular resolution to resolve small-scale (arcminute) polarization fluctuations where weak lensing significantly perturbs the primordial CMB anisotropies.

The BICEP2 and *Keck Array* telescopes, with smaller apertures and beam sizes of $\sim 0.^\circ 5$ at 150 GHz, do not resolve the arcminute-scale fluctuations. Nevertheless, we demonstrate in this paper that the excellent achieved sensitivity makes it possible to perform reconstruction of the lensing potential using only information at larger angular scales and we report a significant detection in the auto-spectrum of the reconstructed lensing potential. In addition, we cross-correlate our reconstructed lensing map with the published *Planck* lensing potential (Planck Collaboration 2015). This cross-spectrum, which is immune to most systematic effects and foregrounds, also detects lensing with high significance. Since the *Planck* lensing potential is reconstructed primarily using temperature, and that from BICEP/*Keck* is reconstructed entirely using polarization, the strong correlation of the two maps shows that they are producing a consistent reconstruction of the true lensing potential. The derived lensing amplitudes are consistent with that expected in the ΛCDM cosmology. Taken together, these results imply that the *B*-mode power in the multipole range of $150 \lesssim \ell \lesssim 350$ previously detected by BICEP/*Keck* (BICEP2/Keck Array Collaboration VI 2015) is indeed caused by lensing.

This paper is part of an on-going series describing results and methods from the BICEP/*Keck* series of experiments (BICEP2 Collaboration I 2014; hereafter BK-I; BICEP2 Collaboration II 2014; hereafter BK-II; BICEP2 Collaboration III 2015; hereafter BK-III; BICEP2 Collaboration IV 2015; hereafter BK-IV; BICEP2/Keck Array Collaborations V 2015; hereafter BK-V; BICEP2 & Planck Collaborations 2015; hereafter BKP; BICEP2/Keck Array Collaboration VI 2015; hereafter BK-VI; BICEP2/Keck Array Collaboration VII 2016; hereafter BK-VII). This paper is organized as follows. In Section 2, we briefly summarize the data sets that are used in this paper, in Section 3, we describe our analysis method for reconstructing the lensing potential from the BICEP/*Keck* data, in Section 4, we give our results including the auto- and cross-spectra of the lensing potential, in Section 5, we present consistency and null tests, and in Section 6, we conclude.

2. OBSERVED DATA AND SIMULATIONS

2.1. BICEP2 and Keck Array

In this paper, we use the BICEP/*Keck* maps, which coadd all data taken up to and including the 2014 observing season—we refer to these as the BK14 maps. These maps were previously described in BK-VI where they were converted to power spectra and used to set constraints on the amplitudes of primordial *B*-modes and foregrounds. In this work, we use only the 150 GHz Q/U map, which have a depth of 3.0 μK-arcmin over an effective area of ~ 395 deg^2, centered on R.A. 0h, decl. $-57.^\circ 5$.

We re-use the standard sets of simulations described in BK-VI and previous papers: lensed and unlensed CMB signal-only simulations (denoted by "lensed-/unlensed-ΛCDM"), instrumental noise, and dust foreground, each having 499 realizations. In addition, in this paper, we also make use of the input lensing potential. The details of the signal and noise simulations are given in Section V of BK-I, and the dust simulations are described in Section IV.A of BKP and Appendix E of BK-VI. As discussed in Section 3, the lensed-ΛCDM, instrumental noise and dust-simulated maps are combined to estimate the transfer function, mean-field bias, disconnected bias, and the uncertainties of the lensing power spectrum. The unlensed-ΛCDM simulations are used to evaluate the significance of detection of lensing (rejection of the no-lensing hypothesis). Lensing is applied to the unlensed input maps using Lenspix (Lewis 2005), as described in Section V.A.2 of BK-I.

Starting with the spherical harmonic coefficients of the input lensing potential (from Lenspix), we first transform to the lensing-mass field κ (lensing convergence) using

$$\kappa_{\rm LM} = -\frac{L(L+1)}{2}\phi_{\rm LM}, \quad (1)$$

and we then make the full-sky κ map by using the spherical harmonic transform of $\kappa_{\rm LM}$. This transformation is necessary to avoid mode mixing in the subsequent apodization to the BK14 sky patch because the lensing-mass field has a nearly flat spectrum, while the lensing potential has a red spectrum (Planck Collaboration 2015). Next, the input lensing-mass map in the BK14 sky patch, $\kappa^{\rm in}(\hat{\boldsymbol{n}})$, is obtained by interpolating the full-sky κ map to the standard BK14 map pixelization and multiplying by the standard inverse variance apodization mask. Here, $\hat{\boldsymbol{n}}$ denotes position in the BK14 sky patch. Finally, the Fourier modes of the input lensing potential in the BK14 sky

patch, $\phi_L^{\rm in}$, are calculated from

$$\phi_L^{\rm in} = -\frac{2}{L^2}\int d^2\hat{\boldsymbol{n}}\; e^{-i\hat{\boldsymbol{n}}\cdot\boldsymbol{L}}\kappa^{\rm in}(\hat{\boldsymbol{n}}). \quad (2)$$

Here and after, we use L for the multipoles of the lensing potential and ℓ for the E and B modes.

2.2. Planck

We use the publicly available *Planck* 2015 lensing-mass field (Planck Collaboration 2015). This lensing-mass field is estimated by optimally combining all of the quadratic estimators constructed from the SMICA temperature and E/B maps. The most effective of the estimators is *TT*, but the *TE* and *EE* estimators also improve the total significance of the detection. We also use the *Planck* 2013 lensing potential (Planck Collaboration 2014a), which has larger statistical uncertainty, but, since it is reconstructed using the temperature maps only, is a useful cross check.

The publicly released *Planck* 2015 lensing package contains multipole coefficients for the observed lensing-mass field, as well as 100 simulated realizations of input and reconstructed lensing-mass fields. The *Planck* 2013 release instead provides multipole coefficients of the unnormalized lensing potential, so we multiply by the provided response function (see Section 2 of Planck Collaboration 2014a) and make a full-sky lensing-mass field. The full-sky *Planck* lensing-mass maps, with point sources masked, are interpolated to the standard BK14 map pixelization. We find that the noise contribution to the *Planck* lensing-mass map in this region is approximately ∼20% smaller than that of the full-sky average due to the scan strategy of the *Planck* mission.

As discussed in Section 3, the *Planck* simulations are used to evaluate the expected correlation between the BK14 and *Planck* lensing signals and its statistical uncertainty. In order to correlate the reconstructed lensing signal between the BK14 and *Planck* simulations, we replace each *Planck* lensing realization with those of the BK14 simulations using (e.g., Giannantonio et al. 2015; Kirk et al. 2016)

$$\widehat{\kappa}^{\rm sim,P'}(\hat{\boldsymbol{n}}) = \widehat{\kappa}^{\rm sim,P}(\hat{\boldsymbol{n}}) - \kappa^{\rm in,P}(\hat{\boldsymbol{n}}) + \kappa^{\rm in}(\hat{\boldsymbol{n}}), \quad (3)$$

where $\kappa^{\rm in,P}$ and $\widehat{\kappa}^{\rm sim,P}$ are the input and reconstructed lensing-mass maps of the *Planck* simulations and $\kappa^{\rm in}$ is the input lensing-mass map of the BK14 realizations. We checked that the correlation between $\widehat{\kappa}^{\rm sim,P'}$ and $\kappa^{\rm in,P}$ is consistent with zero. We then multiply $\widehat{\kappa}^{\rm sim,P'}$ by the standard BK14 inverse variance apodization mask and Fourier transform according to Equation (2).

Hereafter, unless otherwise stated, the *Planck* data refers to the *Planck* 2015 release products.

3. LENSING RECONSTRUCTION METHOD

It is possible to reconstruct the lensing potential from observed CMB anisotropies because lensing introduces off-diagonal mode–mode covariance within and between the *T*-, *E*-, and *B*-mode sets. An estimator of the lensing potential is then given by a quadratic form in the CMB anisotropies. The power spectrum of the lensing potential $C_L^{\phi\phi}$ (lensing potential power spectrum) can be studied by taking the power spectrum of the lensing potential estimator.

In this section, we describe the method used to reconstruct the lensing potential from the BK14 polarization map to calculate the lensing potential power spectrum and to evaluate the amplitudes of the resulting power spectra for the data sets described in Section 2.

3.1. Lensed CMB Anisotropies

The effect of lensing on the Q and U maps is given by (e.g., Lewis & Challinor 2006; Hanson et al. 2010)

$$\begin{aligned}[\widetilde{Q} \pm i\widetilde{U}](\hat{\boldsymbol{n}}) &= [Q \pm iU](\hat{\boldsymbol{n}} + \boldsymbol{d}(\hat{\boldsymbol{n}})) \\ &\simeq [Q \pm iU](\hat{\boldsymbol{n}}) + \boldsymbol{d}(\hat{\boldsymbol{n}})\cdot\boldsymbol{\nabla}[Q \pm iU](\hat{\boldsymbol{n}}),\end{aligned} \quad (4)$$

where $\hat{\boldsymbol{n}}$ is the observed direction and $Q(\widetilde{Q})$ and $U(\widetilde{U})$ are the unlensed (lensed) anisotropies. The two-dimensional vector $\boldsymbol{d}(\hat{\boldsymbol{n}})$ is the deflection angle, with two degrees of freedom. In terms of parity symmetry, these two components are given as the lensing potential (even parity) and curl-mode deflection (odd parity) (Hirata & Seljak 2003b):

$$\boldsymbol{\nabla}^2\phi(\hat{\boldsymbol{n}}) = \boldsymbol{\nabla}\cdot\boldsymbol{d}(\hat{\boldsymbol{n}}), \quad (5)$$

$$(\star\boldsymbol{\nabla})^2\varpi(\hat{\boldsymbol{n}}) = (\star\boldsymbol{\nabla})\cdot\boldsymbol{d}(\hat{\boldsymbol{n}}), \quad (6)$$

where $\boldsymbol{\nabla}$ is the covariant derivative on the sphere and $\star$ denotes the operation that rotates the angle of a two-dimensional vector counterclockwise by 90°.

The E and B modes are defined as

$$E_\ell \pm iB_\ell = -\int \mathrm{d}^2\hat{\boldsymbol{n}} e^{-i\hat{\boldsymbol{n}}\cdot\boldsymbol{\ell}}[Q \pm iU](\hat{\boldsymbol{n}})e^{\mp 2i\varphi_\ell}, \quad (7)$$

where φ_ℓ is the angle of $\boldsymbol{\ell}$ measured from the Stokes Q axis. With the lensing potential and curl mode given in Equations (5) and (6), the lensed E and B modes are given by (e.g., Hu & Okamoto 2002; Cooray et al. 2005)

$$\begin{aligned}\widetilde{E}_\ell &= E_\ell + \int\frac{d^2L}{(2\pi)^2}[\boldsymbol{L}\cdot(\boldsymbol{\ell}-\boldsymbol{L})\phi_{\boldsymbol{L}} + (\star\boldsymbol{L})\cdot(\boldsymbol{\ell}-\boldsymbol{L})\varpi_{\boldsymbol{L}}] \\ &\quad\times E_{\ell-L}\cos 2(\varphi_{\ell-\boldsymbol{L}} - \varphi_\ell),\end{aligned} \quad (8)$$

$$\begin{aligned}\widetilde{B}_\ell &= \int\frac{d^2\boldsymbol{L}}{(2\pi)^2}[\boldsymbol{L}\cdot(\boldsymbol{\ell}-\boldsymbol{L})\phi_{\boldsymbol{L}} + (\star\boldsymbol{L})\cdot(\boldsymbol{\ell}-\boldsymbol{L})\varpi_{\boldsymbol{L}}] \\ &\quad\times E_{\ell-\boldsymbol{L}}\sin 2(\varphi_{\ell-\boldsymbol{L}} - \varphi_\ell).\end{aligned} \quad (9)$$

Because the contribution of B modes from gravitational waves is tightly constrained in the BK-VI paper and rapidly decreases in amplitude at $\ell > 100$, we ignore their possible contribution here.

Up to first order in ϕ and ϖ, the lensing-induced off-diagonal elements of the covariance are (e.g., Hu & Okamoto 2002; Cooray et al. 2005)

$$\langle\widetilde{E}_{\boldsymbol{L}}\widetilde{B}_{\ell-\boldsymbol{L}}\rangle_{\rm CMB} = w^{\phi}_{\ell,\boldsymbol{L}}\phi_\ell + w^{\varpi}_{\ell,\boldsymbol{L}}\varpi_\ell, \quad (10)$$

where $\langle\cdots\rangle_{\rm CMB}$ denotes the ensemble average over unlensed E modes, with a fixed realization of the lensing potential and curl modes. The explicit forms of the weight functions for the lensing potential and curl mode are, respectively, given in Hu & Okamoto (2002) and Namikawa et al. (2012) as

$$w^{\phi}_{\boldsymbol{L},\boldsymbol{\ell}} = -\boldsymbol{\ell}\cdot(\boldsymbol{L}-\boldsymbol{\ell})\widetilde{C}_\ell^{\rm EE}\sin 2(\varphi_\ell - \varphi_{\boldsymbol{L}-\boldsymbol{\ell}}), \quad (11)$$

$$w^{\varpi}_{\boldsymbol{L},\boldsymbol{\ell}} = -(\star\boldsymbol{\ell})\cdot(\boldsymbol{L}-\boldsymbol{\ell})\widetilde{C}^{\rm EE}_{\ell}\sin 2(\varphi_{\boldsymbol{\ell}}-\varphi_{\boldsymbol{L}-\boldsymbol{\ell}}), \quad (12)$$

where $\widetilde{C}^{\rm EE}_{\ell}$ is the lensed E-mode power spectrum to take into account the higher-order biases (Hanson et al. 2011; Lewis et al. 2011). Equation (10) means that the lensing signals, ϕ and ϖ, can be estimated through off-diagonal elements of the covariance matrix of the CMB Fourier modes (see Section 3.3 for details). Note that we do not include ϖ in our simulations because its contribution is negligible in the standard ΛCDM model (e.g., Saga et al. 2015; Pratten & Lewis 2016). We use the reconstructed curl mode as a null test in Section 5.

3.2. Input E- and B-modes for Reconstruction

In BICEP/*Keck* analysis, we use real space matrix operations to process the data into purified E and B maps, which are then transformed to multipole space. The sky signal is filtered by the observing strategy and the analysis process, including the removal of potential systematic errors ("deprojection"). These effects are entirely captured in an *observation matrix*, $\boldsymbol{R}$ (see Tolan 2014 and BK-VII). The observed maps, $Q^{\rm obs}$ and $U^{\rm obs}$, are then given by

$$\begin{pmatrix} Q^{\rm obs} \\ U^{\rm obs} \end{pmatrix} = \boldsymbol{R}\begin{pmatrix} Q' \\ U' \end{pmatrix} + \begin{pmatrix} Q^{\rm noise} \\ U^{\rm noise} \end{pmatrix}. \quad (13)$$

Here Q' and U' are an input signal realization—in this case, lensed-ΛCDM+dust—and the second term is a noise realization. The observed map suffers from some mixing of E and B modes induced by, e.g., the survey boundary and the filtering. To mitigate the mixing between E and B modes, the observed E- and B-*mode* maps are multiplied by purification matrices $\boldsymbol{\Pi}^{E}$ and $\boldsymbol{\Pi}^{B}$, respectively, to recover *pure* E and B modes. This operation is simply expressed as (Tolan 2014)

$$\begin{pmatrix} \widehat{Q}^{E} \\ \widehat{U}^{E} \end{pmatrix} = \boldsymbol{\Pi}^{E}\begin{pmatrix} Q^{\rm obs} \\ U^{\rm obs} \end{pmatrix}, \quad (14)$$

$$\begin{pmatrix} \widehat{Q}^{B} \\ \widehat{U}^{B} \end{pmatrix} = \boldsymbol{\Pi}^{B}\begin{pmatrix} Q^{\rm obs} \\ U^{\rm obs} \end{pmatrix}, \quad (15)$$

where $\widehat{Q}^{E}$ ($\widehat{Q}^{B}$) and $\widehat{U}^{E}$ ($\widehat{U}^{B}$) are purified Stokes Q and U maps containing as much of the original E (B) modes as possible. The Fourier transforms of the purified, apodized Q/U maps are converted to purified E and B modes, $\widehat{E}$ and $\widehat{B}$, and these are used as inputs to the lensing reconstruction analysis.

The input CMB Fourier modes require proper weighting to optimize the lensing reconstruction. In the ideal case (i.e., white noise, full-sky observation with no filtering), the lensing reconstruction is optimized by a simple diagonal weighting of $E_{\boldsymbol{\ell}}$ and $B_{\boldsymbol{\ell}}$. Denoting $X = E$ or B, the optimally weighted Fourier modes are given by (Hu & Okamoto 2002)

$$\overline{X}_{\ell} = \frac{\widehat{X}_{\ell}}{\widehat{C}^{\rm XX}_{\ell}}. \quad (16)$$

Here $\widehat{E}$ and $\widehat{B}$ are, again, the purified E and B modes obtained by the Fourier transform of the purified Q/U maps in Equations (14) and (15), and $\widehat{C}^{\rm XX}_{\ell}$ is an isotropic power spectrum including noise and foregrounds. In more realistic situations, using diagonal filtering degrades the sensitivity to the lensing potential (Hirata & Seljak 2003b; Smith et al. 2007; Hanson & Lewis 2009; Planck Collaboration 2014a). To take into account the anisotropic filtering and noise, we multiply two-dimensional functions in Fourier space to the purified E and B modes

$$\overline{X}_{\ell} \simeq \frac{f^{\rm X}_{\ell}\widehat{X}_{\ell}}{\widehat{C}^{\rm XX}_{\ell}}, \quad (17)$$

where $\widehat{C}^{\rm XX}_{\ell}$ is the mean of the two-dimensional E-/B-mode spectra of the lensed-ΛCDM+dust+noise simulations and the factor $f^{\rm X}_{\ell}$ describes the beam and filtering suppression of the E and B modes. We calculate these suppression factors by comparing the mean input and output power spectra of the lensed-ΛCDM signal-only simulations, $C^{\rm XX,in}_{\ell}$ and $C^{\rm XX,out}_{\ell}$, as $(f^{\rm X}_{\ell})^2 = C^{\rm XX,out}_{\ell}/C^{\rm XX,in}_{\ell}$.

In addition to the above filtering function, we filter in multipole space to select E and B modes with the baseline ranges being $30 \leqslant \ell \leqslant 700$ and $150 \leqslant \ell \leqslant 700$, respectively. The minimum multipole of the E modes is set by the timestream filtering—multipoles smaller than $\lesssim$30 are so heavily attenuated as to be unrecoverable. The minimum multipole of the B modes is chosen so that the dust foreground is subdominant compared to the lensing B modes. The nominal maximum multipole is set by the resolution of the standard BK14 maps which have 0°.25 pixel spacing. We will see later (in Section 5) that restricting to $\ell < 600$ makes very little difference to the final result.

We have not previously published any results for $\ell > 350$ because the beam correction becomes very large, and hence, in principle, so does the uncertainty on that correction. As shown in Figure 1, we find that the mean of the signal simulations actually remains very close to the observed bandpower values for multipoles all the way up to the pixel scale. However, there is a small positive deviation at higher ℓ that reaches 20% at $\ell = 600$, implying that we have slightly underestimated our beam function in this range. This is very clear in the *TT*

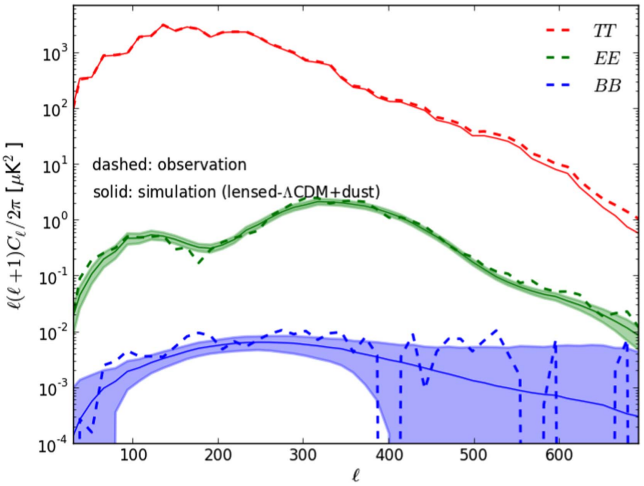

Figure 1. Raw temperature, E- and B-mode spectra (dashed lines) measured from BK14 compared with those from lensed-ΛCDM+dust+noise simulations. (Both have been noise de-biased, but no beam or filtering correction has been applied.) For the simulations, the solid line shows the mean value and the shaded region the $\pm 1\sigma$ range. The temperature sky input to the simulations is constrained to be the actual sky pattern as observed by *Planck* so there is no sample variance in the simulated *TT* spectra.

spectrum, because the input sky for the simulations is constrained to the actual sky pattern as observed by *Planck* (as described in Section V.A.1 of BK-I), and hence, there is no sample variance in this comparison. Based on this observation, we apply a small additional beam correction for the baseline lensing analysis presented in this paper. In practice, we multiply the inverse square root of the ℓ-dependent correction to the observed (and also simulated noise) E/B modes and then compute the weighted Fourier modes of Equation (17). As shown in Section 5, this correction only leads to small changes in the final results.

3.3. Estimating the Lensing Potential

We now describe the estimator for the lensing potential. Equation (10) motivates the following quadratic estimator for the lensing potential (Hu 2001; Hu & Okamoto 2002)

$$\widehat{\phi}_{\boldsymbol{L}} = A_L^{\phi}(\overline{\phi}_{\boldsymbol{L}} - \langle\overline{\phi}_{\boldsymbol{L}}\rangle), \tag{18}$$

where $\langle\cdots\rangle$ is the ensemble average over realizations of purified E and B modes and $\overline{\phi}_{\boldsymbol{L}}$ is the unnormalized EB estimator,

$$\overline{\phi}_{\boldsymbol{L}} = \int \frac{d^2\boldsymbol{\ell}}{(2\pi)^2} w^{\phi}_{\boldsymbol{L},\boldsymbol{\ell}} \overline{E}_{\boldsymbol{\ell}} \overline{B}_{\boldsymbol{L}-\boldsymbol{\ell}}. \tag{19}$$

Here, $w^{\phi}_{\boldsymbol{L},\boldsymbol{\ell}}$ is the weight function given in Equation (11). The second term, $\langle\overline{\phi}_{\boldsymbol{L}}\rangle$, is a correction for the mean-field bias and is estimated from the simulations. The quantities, $\overline{E}$ and $\overline{B}$, are the weighted Fourier modes given in Equation (17), and $A_{\boldsymbol{L}}$ is a normalization that makes the estimator unbiased.

Similarly, the curl-mode estimator is constructed by replacing the weight function with $w^{\varpi}_{\boldsymbol{L},\boldsymbol{\ell}}$, which is given in Equation (12). Up to first order in ϕ and ϖ, the estimator of the lensing potential is unbiased, even in the presence of the curl mode, and vice versa (Namikawa et al. 2012).

Unlike the lensing reconstruction from the temperature and E-mode, the mean-field bias due to the presence of the sky cut is typically small for this EB estimator with an appropriate treatment for E/B mixing (Namikawa & Takahashi 2014; Pearson et al. 2014). Other non-lensing anisotropies could generate a mean-field component (e.g., Hanson et al. 2009), but our simulations show that the mean-field bias is smaller than the simulation noise that corresponds to A_L^{ϕ} divided by the number of realizations (see, e.g., Namikawa et al. 2013). We also note again that our simulated maps are generated with the temperature sky constrained to that observed by *Planck*. However, the use of these constrained realizations results in a contribution in the mean-field bias that is consistent with the simulation noise and therefore has a negligible effect on our results.

In the ideal case, the normalization of the estimator is given analytically by

$$\overline{A}_L^{\phi} = \left\{ \int \frac{d^2\boldsymbol{\ell}}{(2\pi)^2} \frac{|w^{\phi}_{\boldsymbol{L},\boldsymbol{\ell}}|^2}{\widehat{C}^{\rm EE}_{\ell}\widehat{C}^{\rm BB}_{|\boldsymbol{L}-\boldsymbol{\ell}|}} \right\}^{-1}. \tag{20}$$

In BICEP/*Keck*, different CMB multipoles are mixed by the survey boundary and anisotropic filtering. Therefore, we calculate the normalization factor using simulations, as other experiments have done (POLARBEAR Collaboration 2014b; Story et al. 2015; van Engelen et al. 2015). In practice, we use the following additional normalization:

$$A_L^{\phi} = \frac{\langle|\phi^{\rm in}_{\boldsymbol{L}}|^2\rangle}{\langle\phi^{\rm in}_{\boldsymbol{L}}(\widehat{\phi}^{\rm sim}_{\boldsymbol{L}})^*\rangle}\overline{A}_L^{\phi}, \tag{21}$$

where $\phi^{\rm in}_{\boldsymbol{L}}$ and $\widehat{\phi}^{\rm sim}_{\boldsymbol{L}}$ are the input and reconstructed lensing potential from simulation.

3.4. Estimating the Lensing Potential Power Spectrum

We estimate the lensing potential power spectrum using the reconstructed lensing potential from BK14 data alone and also by cross-correlating the reconstructed lensing potential from BK14 with that from *Planck*.

The power spectrum of the lensing potential is estimated by squaring $\widehat{\phi}_{\boldsymbol{L}}$. The lensing potential estimator is quadratic in the CMB, and its power spectrum is the four-point correlation of the CMB anisotropies. This power spectrum can be decomposed into the disconnected and connected parts

$$\langle|\widehat{\phi}_{\boldsymbol{L}}|^2\rangle = \langle|\widehat{\phi}_{\boldsymbol{L}}|^2\rangle_{\rm C} + \langle|\widehat{\phi}_{\boldsymbol{L}}|^2\rangle_{\rm D}. \tag{22}$$

The disconnected part $|\widehat{\phi}_{\boldsymbol{L}}|^2_{\rm D}$ comes from the Gaussian part of the four-point correlation, while the connected part contains the non-Gaussian contributions from lensing. The connected part gives the lensing power spectrum, $C_L^{\phi\phi}$, with a correction from the higher-order bias (Kesden et al. 2003), which is negligible in our analysis. On the other hand, the disconnected part of the four-point correlation remains even in the absence of lensing and is given by

$$\begin{aligned}\langle|\widehat{\phi}|^2_{\boldsymbol{L}}\rangle_{\rm D} = (A_L^{\phi})^2 \int \frac{d^2\boldsymbol{\ell}}{(2\pi)^2}\int \frac{d^2\boldsymbol{\ell}'}{(2\pi)^2} w^{\phi}_{\boldsymbol{L},\boldsymbol{\ell}} w^{\phi}_{-\boldsymbol{L},\boldsymbol{\ell}'} \\ \times [\overline{\boldsymbol{C}}^{\rm EE}_{\boldsymbol{\ell},\boldsymbol{\ell}'}\overline{\boldsymbol{C}}^{\rm BB}_{\boldsymbol{L}-\boldsymbol{\ell},-\boldsymbol{L}-\boldsymbol{\ell}'} + \overline{\boldsymbol{C}}^{\rm EB}_{\boldsymbol{\ell},\boldsymbol{L}-\boldsymbol{\ell}'}\overline{\boldsymbol{C}}^{\rm EB}_{\boldsymbol{\ell}',-\boldsymbol{L}-\boldsymbol{\ell}}],\end{aligned} \tag{23}$$

where A_L^{ϕ} is the angle average of the estimator normalization in Equation (21) and $\overline{\boldsymbol{C}}^{XY}_{\boldsymbol{\ell},\boldsymbol{\ell}'} \equiv \langle\overline{X}_{\boldsymbol{\ell}}\overline{Y}_{\boldsymbol{\ell}'}\rangle$ is the covariance matrix. The disconnected part of the four-point correlation is produced by both the CMB fluctuations and instrumental noise. We describe the treatment of the disconnected bias for auto- and cross-lensing power in the next two sections.

3.4.1. Auto-spectrum of BK14

For the auto-spectrum of the BK14 lensing potential, the disconnected bias is a significant contribution that must be subtracted. The de-biased lensing potential power spectrum is given by

$$\widehat{C}_{\boldsymbol{L}}^{\phi\phi} \equiv |\widehat{\phi}_{\boldsymbol{L}}|^2 - \widehat{N}^{\phi}_{\boldsymbol{L}}, \tag{24}$$

where $\widehat{N}^{\phi}_{\boldsymbol{L}}$ is the disconnected bias, and a normalization factor (the correction for the apodization window) is omitted for clarity. In principle, this Gaussian bias can be estimated from the explicit formula in Equation (23) or dedicated Gaussian simulations. However, these approaches rely on an accurate model of $\overline{\boldsymbol{C}}^{XY}_{\boldsymbol{\ell},\boldsymbol{\ell}'}$. Using an inaccurate covariance matrix, $\overline{\boldsymbol{C}}^{XY} + \Sigma^{XY}$, Equation (23) results in an error $\mathcal{O}(\Sigma^{XY})$.

In our analysis, the disconnected bias is estimated with the *realization-dependent* method developed by Namikawa et al. (2013) for temperature and extended by Namikawa & Takahashi (2014) to include polarization. In this method, part

of the covariance is replaced with the real data and is given by

$$\widehat{N}^{\phi}_{\boldsymbol{L}} = \langle|\widehat{\phi}^{E_1,\widehat{B}}_{\boldsymbol{L}} + \widehat{\phi}^{\widehat{E},B_1}_{\boldsymbol{L}}|^2\rangle_1 - \frac{1}{2}\langle|\widehat{\phi}^{E_1,B_2}_{\boldsymbol{L}} + \widehat{\phi}^{E_2,B_1}_{\boldsymbol{L}}|^2\rangle_{1,2}. \quad (25)$$

Here, $\widehat{\phi}^{XY}_{\boldsymbol{L}}$ is the lensing estimator computed from the quadratic combination of X and Y. $\widehat{E}$ and $\widehat{B}$ are the purified E and B modes from real data, while E_1 (E_2) and B_1 (B_2) are generated from the first (second) set of simulations. The ensemble average $\langle\cdots\rangle_i$ is taken over the i'th set of simulations. Our simulation set is divided into two subsets multiple times to estimate the second term.

Note that this form of disconnected bias is obtained naturally from the optimal estimator for the lensing-induced trispectrum using the Edgeworth expansion of the CMB likelihood (Appendix A). Realization-dependent methods have the benefit of suppressing spurious off-diagonal elements in the covariance matrix. Furthermore, the disconnected bias estimated using this method is less sensitive to the accuracy of the covariance, i.e., it contains contributions from $\mathcal{O}(\Sigma^2)$ instead of $\mathcal{O}(\Sigma)$.

The curl-mode power spectrum is also estimated in the same way, but with the quadratic estimator of the curl-mode $\widehat{\varpi}_{\boldsymbol{L}}$, while the disconnected bias becomes very small in estimating the cross-spectrum between the lensing potential and curl mode.

3.4.2. Cross-spectrum with Planck

In cross-correlation studies involving *Planck*, we expect the disconnected bias in cross-spectra to be completely negligible. The reasons are as follows.

In cross-spectrum analysis, the instrumental noise of the two experiments is uncorrelated. Disconnected bias can only arise from sky signal. The *Planck* 2015 lensing potential is estimated from all of the quadratic estimators, including those involving polarization. Therefore, even in the absence of lensing, two of these quadratic estimators (the *EB* and *TB* estimators) are correlated with the *EB* estimator computed from the BK14 data through the common sky signal.

In practice, this disconnected bias is small. The correlation of *B* modes between these two experiments does not contain noise contributions. The four-point correlation, *EBEB* and *TBEB*, are then produced by the CMB *B*-mode signals, but not by the instrumental noise in *B* modes. The uncertainties in the *Planck* lensing potential are dominated by instrumental noise, which is much larger than any possible *B* modes on the sky that can lead to a disconnected bias. To see this more quantitatively, we evaluate the disconnected bias expected from the ΛCDM *B*-mode power spectrum and appropriate noise levels, using the analytic formula based on Hu & Okamoto (2002). We find that the bias is indeed negligible compared to the reconstruction noise (see Figure 5).

In addition, since the *Planck* 2013 lensing potential is reconstructed from the temperature maps alone, the cross-spectrum between BK14 and *Planck* 2013 is free of any disconnected bias. In the next section, we show that the cross-spectrum results with *Planck* 2013 and *Planck* 2015 are consistent, again confirming that the disconnected bias in the *Planck* 2015—BK14 cross-spectrum is not significant.

3.4.3. Binned Power Spectrum and Its Amplitude

In our analysis, the multipoles between 30 and 700 are divided into 10 bins and the bandpowers of the lensing potential power spectrum C_b are given at these multipole bins. We estimate the amplitude of the lensing potential power spectrum as a weighted mean over multipole bins

$$A^{\phi\phi}_{\rm L} = \frac{\sum_b a_b A_b}{\sum_b a_b}, \quad (26)$$

where A_b is the relative amplitude of the power spectrum compared with a fiducial power spectrum C^f_b, i.e., $A_b \equiv C_b/C^f_b$, and the weights, a_b, are taken from the bandpower covariance according to

$$a_b = \sum_{b'} C^f_b \boldsymbol{Cov}^{-1}_{bb'} C^f_{b'}. \quad (27)$$

The fiducial bandpower values and their covariances are evaluated from the simulations. Consequently, $A^{\phi\phi}_{\rm L}$ defined as above is an amplitude relative to the *Planck* ΛCDM prediction.

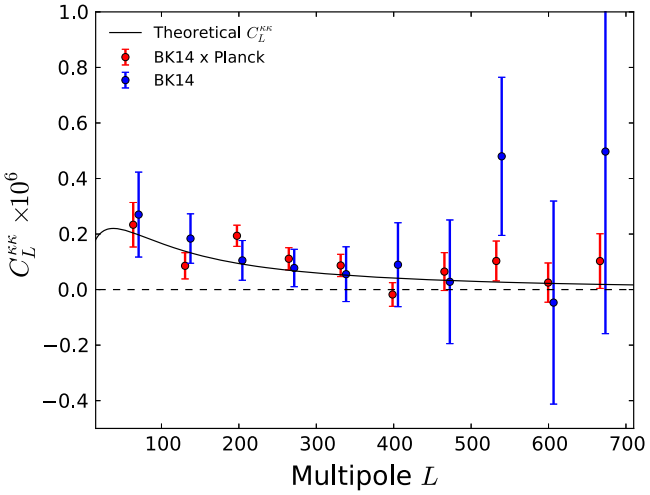

Figure 2. Lensing-mass power spectrum, $C_L^{\kappa\kappa} = L^4 C_L^{\phi\phi}/4$, estimated from the cross-spectrum between BK14 and *Planck* 2015 data (red), and the auto-spectrum of BK14 data (blue). The black solid line shows the theoretical spectrum assuming the ΛCDM cosmology. The BK14 auto-spectrum is offset in L for clarity.

Table 1
The Bandpowers of the Lensing-mass Power Spectrum and 1σ Statistical Errors at the Center of Each Bin, $L_{\rm c}$, as Shown in Figure 2

$L_{\rm c}$	BK14 × *Planck*	BK14
63.5	2.33 ± 0.80	2.70 ± 1.53
130.5	0.86 ± 0.47	1.84 ± 0.89
197.5	1.94 ± 0.38	1.05 ± 0.72
264.5	1.11 ± 0.40	0.78 ± 0.67
331.5	0.87 ± 0.40	0.55 ± 0.99
398.5	−0.18 ± 0.43	0.90 ± 1.51
465.5	0.65 ± 0.68	0.28 ± 2.23
532.5	1.03 ± 0.72	4.80 ± 2.85
599.5	0.25 ± 0.71	−0.47 ± 3.66
666.5	1.03 ± 0.98	4.97 ± 6.56

Note. The values of the bandpowers and errors are multiplied by 10^7.

4. RESULTS

Figure 2 shows the cross-spectrum of the BK14 and *Planck* lensing-mass fields and the auto-spectrum of the BK14 data alone. Table 1 shows the bandpowers and 1σ

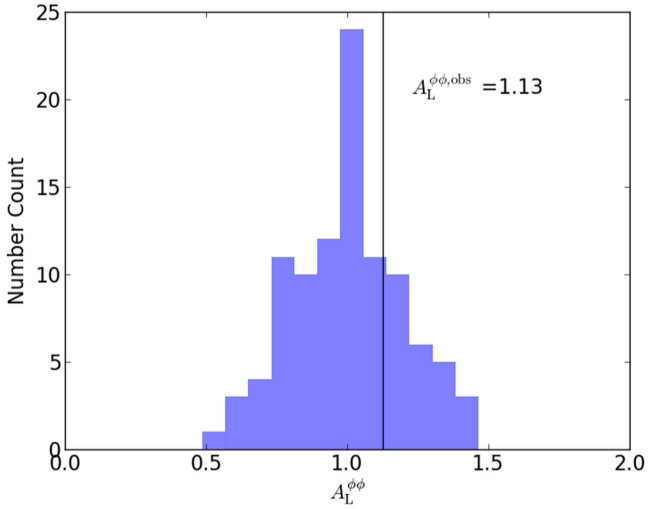

Figure 3. Amplitudes of the cross-spectra of BK14 and *Planck* 2015 lensing potential maps reconstructed from lensed-ΛCDM+dust+noise simulations (histogram), and the observed value (vertical line).

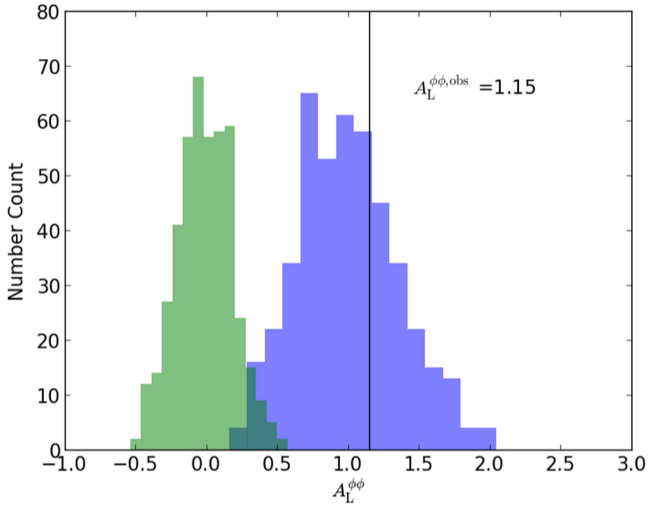

Figure 4. Amplitudes of the auto-spectra of BK14 lensing potential maps reconstructed from lensed-ΛCDM+dust+noise simulations (blue histogram), and from unlensed-ΛCDM+dust+noise simulations (green histogram). The observed value is indicated by the vertical line.

statistical errors of the lensing power spectrum. Figure 3 compares the amplitude of the lensing cross-spectrum between BK14 and *Planck* to lensed-ΛCDM+dust+noise simulations, while the line and blue histogram in Figure 4 do the same thing for the BK14 auto-spectrum. The observed amplitude estimated from the cross-spectrum is $A_{\rm L}^{\phi\phi} = 1.13 \pm 0.20$, and the amplitude estimated from the auto-spectrum is $A_{\rm L}^{\phi\phi} = 1.15 \pm 0.36$. In each case, the uncertainty is taken from the standard deviation of the lensed-ΛCDM+dust+noise simulations. We find that these values are mutually consistent and are also consistent with the *Planck* ΛCDM expectation within the 1σ statistical uncertainty.

To evaluate the rejection significance of the no-lensing hypothesis in Figure 4, we also show the results of a special set of unlensed-ΛCDM+dust+noise simulations where there is no sample variance on the lensing component. Assuming Gaussian statistics we find that the no-lensing hypothesis is rejected at 5.8σ, which is the highest significance achieved to date using *EB* lensing estimator.

The *B*-mode power spectrum can also be used to constrain the amplitude of the lensing effect, and in BKP we quoted the value $A_{\rm L}^{\rm BB} = 1.13 \pm 0.18$ when marginalizing over r and the dust foreground amplitude. Updating to the BK14 spectrum and setting $r = 0$ we find $A_{\rm L}^{\rm BB} = 1.20 \pm 0.17$. The agreement of this result with that from the lensing reconstruction described above verifies that the *B* mode observed by the BICEP/*Keck* experiments at intermediate angular scales is dominated by gravitational lensing.

To show that the disconnected bias in the cross-spectrum is small, an analytic estimate multiplied by $10\times$ for clarity is compared in Figure 5 to the BK14/*Planck* 2015 cross-spectrum. The inclusion of this bias changes the value of the lensing amplitude by less than 1%. In addition, we show an alternate cross-spectrum taken between BK14 and the *Planck* 2013 data. As mentioned earlier, the BK14 and *Planck* 2013 cross-spectrum is free of any disconnected bias. Therefore, the similarity of these two spectra also suggests that the disconnected bias in the BK14 and *Planck* 2015 cross-spectrum is small.

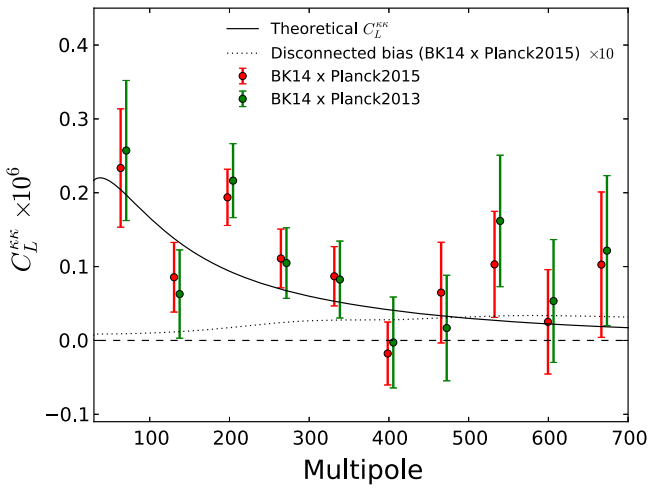

Figure 5. Lensing-mass power spectrum, $C_L^{\kappa\kappa} = L^4 C_L^{\phi\phi}/4$, estimated from the cross-spectrum between BK14 and *Planck* 2015 data compared with that between BK14 and *Planck* 2013 data. We also show the theoretical expectation of the disconnected bias in the cross-spectrum between the BK14 and *Planck* 2015 data multiplied by 10. The cross-spectrum between BK14 and *Planck* 2013 is offset in L for clarity.

5. CONSISTENCY CHECKS AND NULL TESTS

In this section, we discuss systematics in the reconstructed lensing potential. *B* modes in the *EB* estimator for ϕ are an order of magnitude fainter than the *E* modes and need to be tested for non-negligible contributions from systematics or leakage from *E* modes. The matrix-purified BK14 *E* and *B* modes up to $\ell \simeq 350$ used in this paper have already passed the long list of systematics and null tests described in BK-I, BK-III, and BK-VI. In the baseline results presented above we include additional modes up to $\ell_{\rm max} = 700$, and we see below that the modes in the range $350 < \ell < 600$ carry a significant portion of the total available statistical weight. In this section, we therefore discuss additional tests that demonstrate the robustness of the reconstructed ϕ map and the lensing spectrum. Furthermore, note that the cross-spectrum of BK14 and *Planck*, which produces the most stringent constraint on $A_{\rm L}^{\phi\phi}$ in this

Table 2
Probability to Exceed a χ^2 Statistic for the Curl Null Test and the Jackknife Tests

	BK14 × *Planck*		BK14		
	$\phi \times \phi$	$\varpi \times \phi$	$\phi \times \phi$	$\varpi \times \phi$	$\varpi \times \varpi$
Curl	⋯	0.77	⋯	0.92	0.34
Deck	0.51	0.48	0.34	0.06	0.12
Scan Dir	0.37	0.43	0.87	0.15	0.57
Tag Split	0.30	0.85	0.36	0.86	0.73
Tile	0.30	0.16	0.20	0.05	0.54
Phase	0.69	0.68	0.92	0.76	0.25
Mux Col	0.18	0.22	0.46	0.38	0.35
Alt Deck	0.18	0.72	0.39	0.16	0.16
Mux Row	0.49	0.80	0.60	0.58	0.09
Tile/Deck	0.20	0.36	0.83	0.84	0.88
Focal Plane inner/outer	0.09	0.12	0.41	0.35	0.28
Tile top/bottom	0.84	0.51	0.51	0.77	0.28
Tile inner/outer	0.31	0.05	0.91	0.64	0.78
Moon	0.02	0.84	0.18	0.53	0.83
A/B offset best/worst	0.93	1.00	0.57	0.24	0.59

paper, is immune to additive bias from all known systematics and is highly insensitive to the dust foreground.

5.1. Null Tests

In the following, we present results of (i) a curl null test and (ii) jackknife tests that are expected to be consistent with zero unless there are systematics remaining in the data.

To test this quantitatively, we use the probability to exceed (PTE) the value of χ^2 obtained from observations, under the assumption that the fiducial power spectrum is zero in all multipole bins. The PTE is evaluated from the simulation set with the same method as in the BK-I paper. Table 2 summarizes the PTE values obtained. Figure 7 shows the distribution of the jackknife χ^2 PTE.

5.1.1. Curl Null Test

The curl mode is mathematically similar to lensing but cannot be generated by scalar perturbations at linear order. As described in Section 3, the curl mode is estimated by replacing the weight function with $w^{\varpi}_{\ell,\boldsymbol{L}}$, and the reconstruction noise level in the curl mode is similar to that in the lensing potential. It is therefore commonly used as an important check for any residual systematics in lensing reconstruction analysis.

Figure 6 shows the cross-spectrum between the BK14 curl mode and the *Planck* lensing potential, the BK14 curl-mode auto-spectrum, and the cross-spectrum between the BK14 lensing potential and curl mode. For illustrative purposes, similar to the relationship between κ and ϕ, we define $\psi_{\boldsymbol{L}} = -L^2\varpi_{\boldsymbol{L}}/2$ and show the power spectrum of ψ instead of ϖ. We compute the corresponding PTEs for these power spectra (see Table 2), finding no evidence of systematics in these curl null tests.

5.1.2. Jackknife Tests

As part of our standard data reduction, we form multiple pairs of jackknife maps, which split the data into approximately equal halves and which should contain (nearly) identical sky signals, but which might be expected to contain different systematic contamination. We then difference these pairs of

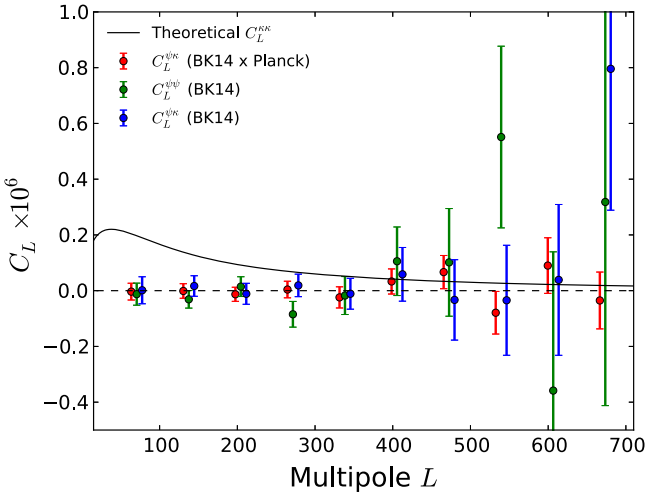

Figure 6. *Curl null test*: cross-spectrum of the curl mode reconstructed from BK14 data and the *Planck* lensing-mass field (red), the auto-spectrum of the BK14 curl mode (green), and the cross-spectrum of the BK14 lensing-mass field and curl mode (blue). For comparison, we also show the theoretical lensing-mass power spectrum (black). The power spectra are offset in L for clarity.

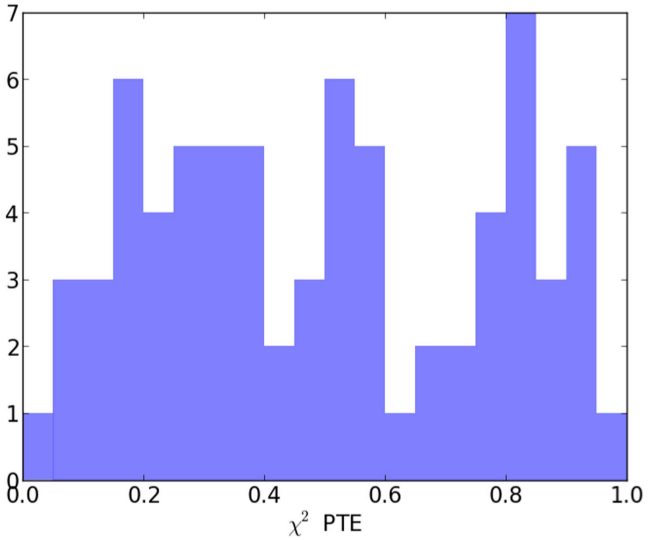

Figure 7. Distribution of the jackknife χ^2 PTE values.

maps and search for signals that are inconsistent with the noise expectation—see BK-I, BK-III, and BK-VI for further details. Here we take these jackknife maps, perform the lensing reconstruction on them, and as usual look for signals that are inconsistent with null.

Table 2 gives the PTE values. We find no evidence of spurious signals in the lensing potential.

5.2. Consistency Checks

As consistency checks of the BK14 lensing potential, we calculate the lensing power spectrum while varying the following analysis choices from their baseline values and give the resulting alternate values of $A_{\rm L}^{\phi\phi}$ in Table 3.

1. Maximum multipole: $\ell_{\rm max}$ in our baseline analysis, the nominal maximum multipole of the E and B modes used for the lensing reconstruction in Equation (19) is $\ell_{\rm max} = 700$. Reducing the value of $\ell_{\rm max}$ to 650 and

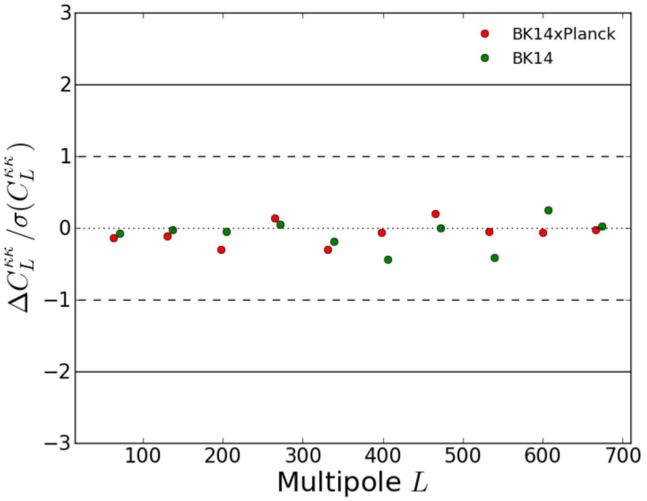

Figure 8. Difference of the lensing power spectrum when subtracting from the BK14 Q/U maps a nominal undeprojected residual as derived from per-channel beam maps (red: BK14 × *Planck*, blue:BK14), divided by the 1σ statistical uncertainty.

Table 3
The Amplitude of the Lensing Potential Power Spectrum $A_L^{\phi\phi}$ Estimated with Different Analysis Choices

	BK14 × *Planck*	BK14
Baseline	1.13 ± 0.20	1.15 ± 0.36
$\ell_{max} = 650$	1.07 ± 0.20	1.21 ± 0.36
$\ell_{max} = 600$	1.14 ± 0.20	1.26 ± 0.36
$\ell_{max} = 350$	1.41 ± 0.30	1.97 ± 0.84
$\ell_{min} = 150$	1.13 ± 0.20	1.14 ± 0.36
$\ell_{min} = 200$	1.07 ± 0.20	0.95 ± 0.40
$\ell^B_{max} = 350$	1.24 ± 0.22	1.33 ± 0.45
Diff. beam ellipticity	1.11 ± 0.20	1.14 ± 0.36
Beam correction	1.18 ± 0.20	1.30 ± 0.36
Apodization	1.07 ± 0.22	0.99 ± 0.39

600, we see small changes in the constraint on $A_L^{\phi\phi}$. However, if we reduce ℓ_{max} to 350 to match the range probed by jackknife tests in BK-VI, the values of $A_L^{\phi\phi}$ shift up, and the statistical errors increase. To quantify how likely the up-shifts are to occur by chance, we compute the corresponding shifts when making the same change in the simulations and find a positive shift greater than the observed one 10% of the time for the cross-spectrum and 15% of the time for the auto-spectrum.

2. Minimum multipole: ℓ_{min} for the baseline analysis the minimum multipole of the E modes is set to 30 in Equation (19) (due to the timestream filtering), while the minimum multipole of the B modes is set to 150 (to ensure that the contributions of the dust foreground is small compared to the noise and lensing signal). Raising ℓ_{min} for the E modes to 150 we see very small changes to the $A_L^{\phi\phi}$ results, while raising both to 200 we see modest changes.
3. Maximum multipole of the B-mode polarization: ℓ^B_{max} as mentioned above, B modes are used up to a nominal $\ell_{max} = 700$ in our baseline analysis. The B-mode polarization at $\ell \gtrsim 350$ is not as well tested against various systematics. However, unlike E modes, B modes at smaller scales $\ell > 350$ do not contribute significantly in estimating $A_L^{\phi\phi}$ (e.g., Simard et al. 2015). We repeat the analysis removing B modes at $\ell > 350$ and find only a moderate change in the results and their statistical uncertainties.
4. Apodization: to mitigate the noisy regions around the survey boundary, our standard analysis applies an inverse variance apodization window. To see how the weighting to pixel values change the results, we also perform the analysis using the sine apodization defined in Namikawa & Takahashi (2014), and find a small change in the results. To quantify how likely the up-shifts are to occur by chance, we computed the corresponding shifts when making the same change in the simulations, and find a positive shift greater than the observed one 81% of the time for the cross-spectrum and 90% of the time for the auto-spectrum.

5.3. Effects of Beam Systematics

Beam shape mismatch of each detector pair leads to a leakage from the bright temperature anisotropies into polarization (e.g., Hu et al. 2003; Miller et al. 2008; Su et al. 2009). In our analysis, this leakage is mitigated by deprojecting (or for ellipticity, subtracting) several modes corresponding approximately to the difference of two elliptical Gaussians (see BK-III for details). To assess the level of leakage remaining after deprojection, we use calibration data consisting of high precision, per-detector beam maps described in BK-IV. In special simulations, we explicitly convolve these beam maps onto an input T sky and process the resulting simulated timestream in the normal manner, including deprojection, to produce maps of the "undeprojected residual." In BK-V, this residual was treated as an upper limit to possible residual systematics. Here, as an additional check, we try subtracting this nominal residual from the maps and re-extracting the lensing potential. Figure 8 shows the differences in the resulting spectrum in units of the bandpower uncertainties, finding that the difference is small compared to the 1σ statistical uncertainty.

In addition to temperature-to-polarization leakage caused by beam mismatch, beam asymmetry as well as detector-to-detector beam shape variation can produce a spurious lensing signal if non-uniform map coverage leads to an effective beam that is spatially dependent (e.g., Planck Collaboration 2014a). The beam map simulation procedure described above does not probe this effect in the EB estimator because the input maps do not contain polarization. However, we note that ellipticity is the dominant component of beam asymmetry and beam shape variation in BICEP2 and *Keck* (see BK-IV, Table 2). We also note that beam ellipticity is a strong function of radial position in the focal plane (see BK-IV, Figures 12–13) so that the focal plane inner/outer jackknife listed in Table 2 is a good proxy for a beam ellipticity jackknife. The fact that this null test passes limits the contribution from beam asymmetry and beam variation to less than the uncertainty.

In our pair-differencing analysis, differences in the beam shapes between the A and B detectors of each pair generates temperature-to-polarization leakage. We filter out the leading order modes of this leakage using a technique that we call deprojection (see BK-III for details). For differential beam ellipticity, however, we do not use deprojection because it

introduces a bias in *TE*. Instead, in our standard analysis, we subtract the expected temperature-to-polarization leakage based on the measured differential beam ellipticity. To test whether the lensing results are sensitive to differential beam ellipticity, we repeat the lensing reconstruction from maps *without* this subtraction and find only a very small change in the results (see Table 3).

We finally test the effects of the beam correction to E/B modes based on the observed level of temperature anisotropies at high ℓ (Section 3). We repeat the same lensing reconstruction without the beam correction and estimate the lensing amplitude. We find that $A_{\rm L}^{\phi\phi}$ increases while the statistical error is unchanged compared to the baseline results, and the differences of $A_{\rm L}^{\phi\phi}$ are $\Delta A_{\rm L}^{\phi\phi} = 0.05$ for BK14 $\times$ *Planck* and $\Delta A_{\rm L}^{\phi\phi} = 0.15$ for BK14 (see Table 3). These changes are within the 1σ statistical error.

5.4. Effects of Absolute Calibration Error

Although the lensing potential is, in principle, a dimensionless quantity, the measured lensing potential depends on the overall amplitude of the polarization map. The calibration uncertainties in E and B modes therefore propagate into an error in the amplitude of the lensing potential spectrum (e.g., POLARBEAR Collaboration 2014b). The absolute calibration uncertainty, δ, is 1.3% in the BICEP2/*Keck* polarization maps (BK-I). Given this uncertainty on amplitudes of the E and B modes, the resultant systematic uncertainties in the lensing spectral amplitudes are $\Delta A_{\rm L}^{\phi\phi} = 4\delta = 0.052$ for the BK14 auto-spectrum and $\Delta A_{\rm L}^{\phi\phi} = 2\delta = 0.026$ for the cross-spectrum with *Planck*, significantly smaller than the statistical uncertainties. Since the estimate of the curl-mode power spectrum is also affected in the same manner, non-detection of the curl mode also indicates that the effect of these uncertainties is negligible compared to the statistical errors.

6. CONCLUSIONS

In this paper, we have reconstructed the lensing potential from the BK14 polarization data and taken its cross-spectrum with the public *Planck* lensing potential, as well as the auto-spectrum of the BK14 alone. The amplitude of the cross-spectrum with *Planck* is constrained to be $A_{\rm L}^{\phi\phi} = 1.13 \pm 0.20$, while the auto-spectrum has the amplitude $A_{\rm L}^{\phi\phi} = 1.15 \pm 0.36$. By comparing the auto-spectrum to special unlensed simulations, we reject the no-lensing hypothesis at 5.8σ significance, which is the highest significance achieved to date using *EB* lensing estimator. We have performed several consistency checks and null tests and find no evidence for spurious signals in our reconstructed map and spectra.

This paper demonstrates for the first time lensing reconstruction using B modes in the intermediate multipole range ($\ell = 150$–350). The results verify that the B-mode power observed by the BICEP/*Keck* experiments on these intermediate angular scales is dominated by gravitational lensing. The good agreement between these results and $A_{\rm L}^{\rm BB} = 1.20 \pm 0.17$ from the BK14 B-mode spectrum starts to place constraints on any alternative sources of B modes at these angular scales, such as cosmic strings (e.g., Seljak & Slosar 2006; Pogosian & Wyman 2008), primordial magnetic fields (e.g., Shaw & Lewis 2010; Bonvin et al. 2014), and cosmic birefringence induced by interaction between a massless pseudo-scalar field and photons (e.g., Pospelov et al. 2009; Lee et al. 2015; POLARBEAR Collaboration 2015). The calculation of formal quantitative constraints is rather involved and depends on the assumed statistical properties of the alternative B-mode sources. We leave that to future work.

Looking ahead, the reconstructed lensing potential can be used to cross-correlate with other astronomical tracers. However, the reconstruction noise of the BICEP/*Keck* data will limit its usefulness as a cosmological probe in the era of DES (The Dark Energy Survey Collaboration 2016), DESI (The DESI Collaboration 2013), and LSST (LSST Dark Energy Science Collaboration 2012). As the sensitivity of BICEP/*Keck* improves, our main objective is to use a well-measured deflection map ϕ to form a degree-scale B-mode lensing template, which can then be used to improve our final uncertainties on r (i.e., "delensing"). Multiple studies have shown that high resolution CMB polarization data (e.g., Seljak & Hirata 2004; Smith et al. 2012), the CIB (Sherwin & Schmittfull 2015; Simard et al. 2015), galaxy clustering (Namikawa et al. 2016), or weak lensing (Sigurdson & Cooray 2005; Marian & Bernstein 2007) can all improve measurements of ϕ. In addition to the lensing potential presented here, there already exists in the BICEP/*Keck* field data from the *Planck* CIB measurements (Planck Collaboration 2014b, 2014c) as well as high resolution CMB maps from SPTPOL. We are exploring the formation of a lensing template using an optimal combination of these and anticipate using this in our likelihood analysis in the near future. This template will considerably improve as SPT3G (Benson et al. 2014) comes online.

The *Keck Array* project has been made possible through support from the National Science Foundation under Grants ANT-1145172 (Harvard), ANT-1145143 (Minnesota), and ANT-1145248 (Stanford), and from the Keck Foundation (Caltech). The development of antenna-coupled detector technology was supported by the JPL Research and Technology Development Fund and grant Nos. 06-ARPA206-0040 and 10-SAT10-0017 from the NASA APRA and SAT programs. The development and testing of focal planes were supported by the Gordon and Betty Moore Foundation at Caltech. Readout electronics were supported by a Canada Foundation for Innovation grant to UBC. The computations in this paper were run on the Odyssey cluster supported by the FAS Science Division Research Computing Group at Harvard University. The analysis effort at Stanford and SLAC is partially supported by the U.S. Department of Energy Office of Science. We thank the staff of the U.S. Antarctic Program and in particular the South Pole Station without whose help this research would not have been possible. Special thanks go to our heroic winter-overs Robert Schwarz and Steffen Richter. We thank all those who have contributed past efforts to the BICEP-*Keck Array* series of experiments, including the BICEP1 team. T.N. acknowledges support from Japan Society for the Promotion of Science Postdoctoral Fellowships for Research Abroad.

APPENDIX
DISCONNECTED BIAS ESTIMATION

The realization-dependent method for the disconnected bias given in Equation (33) comes naturally from deriving the optimal estimator for the lensing-induced trispectrum. Here we

briefly summarize derivation of Equation (33) (see Appendix A of Namikawa & Takahashi 2014 for a thorough derivation).

The lensing-induced trispectrum that is relevant to our analysis is given by (see, e.g., Lewis & Challinor 2006)

$$T_{\ell_1\ell_2\ell_3\ell_4} \equiv \langle E_{\ell_1} B_{\ell_2} E_{\ell_3} B_{\ell_4}\rangle_{\rm C} \simeq \delta^D_{\ell_1+\ell_2+\ell_3+\ell_4}\,[w^{\phi}_{\ell_1+\ell_2,\ell_1} w^{\phi}_{\ell_3+\ell_4,\ell_3} C^{\phi\phi}_{|\ell_1+\ell_2|} + w^{\phi}_{\ell_1+\ell_4,\ell_1} w^{\phi}_{\ell_2+\ell_3,\ell_2} C^{\phi\phi}_{|\ell_1+\ell_4|}], \quad (28)$$

where $w^{\phi}_{\boldsymbol{L},\boldsymbol{\ell}}$ is given in Equation (11), $C^{\phi\phi}_L$ is the lensing potential power spectrum, and $\delta^D_{\boldsymbol{L}}$ is the Dirac delta function in Fourier space. In the Edgeworth expansion of the E- and B-mode likelihood, the term containing the above trispectrum is given by (Regan et al. 2010)

$$\mathcal{L} \propto \left[\prod_{i=1}^{4}\int\frac{d^2\boldsymbol{\ell}_i}{(2\pi)^2}\right] T_{\ell_1\ell_2\ell_3\ell_4}\frac{\partial}{\partial E_{\ell_1}}\frac{\partial}{\partial B_{\ell_2}}\frac{\partial}{\partial E_{\ell_3}}\frac{\partial}{\partial B_{\ell_4}}\mathcal{L}_{\rm g}, \quad (29)$$

where $\mathcal{L}_{\rm g}$ is the Gaussian likelihood of the E and B mode:

$$\mathcal{L}_{\rm g} \propto \exp\left(-\frac{1}{2}\left[\prod_{i=1}^{2}\int\frac{d^2\boldsymbol{\ell}_i}{(2\pi)^2}\right]\sum_{a,b=E,B} a_{\ell_1}\{\boldsymbol{C}^{-1}\}^{a_{\ell_1}b_{\ell_2}} b_{\ell_2}\right). \quad (30)$$

Here, $\{\boldsymbol{C}\}^{a_\ell b_\ell} = \langle a_\ell b_{\ell'}\rangle$ is the covariance matrix and we omit the normalization of the above Gaussian likelihood.

The optimal estimator for the lensing power spectrum in the trispectrum is obtained by maximizing the CMB likelihood. The approximate formula that is numerically tractable is proportional to the derivative of the log-likelihood with respect to $C^{\phi\phi}_L$. The derivative of the above likelihood with respect to the lensing potential power spectrum is given by (Namikawa & Takahashi 2014)

$$\frac{\partial\mathcal{L}}{\partial C^{\phi\phi}_L} \propto \left[\prod_{i=1}^{2}\int\frac{d^2\boldsymbol{\ell}_i}{(2\pi)^2}\right] w^{\phi}_{\boldsymbol{L},\boldsymbol{\ell}_1} w^{\phi}_{-\boldsymbol{L},\ell_2}\frac{\partial}{\partial E_{\ell_1}}\frac{\partial}{\partial B_{\boldsymbol{L}-\ell_1}}\frac{\partial}{\partial E_{\ell_2}} \times \frac{\partial}{\partial B_{-\boldsymbol{L}-\ell_2}}\mathcal{L}_{\rm g} \simeq \left(|\overline{\phi}^{EB}_{\boldsymbol{L}}|^2 - \frac{\widehat{N}^{\phi}_{\boldsymbol{L}}}{(A^{\phi}_L)^2}\right)\mathcal{L}_{\rm g}. \quad (31)$$

After correcting the normalization for the unbiased estimator, the above equations leads to Equation (24).

Realization-dependent methods are useful to suppress spurious off-diagonal elements in the covariance matrix of the power spectrum estimates (e.g., Dvorkin & Smith 2009; Hanson et al. 2011). As discussed in Namikawa et al. (2013), the disconnected bias estimation described above is less sensitive to errors in covariance compared to the other approaches. To see this, using Equation (18), we rewrite Equation (23) as

$$\widehat{N}^{\phi}_{\boldsymbol{L}} = (A^{\phi}_L)^2\int\frac{d^2\boldsymbol{\ell}}{(2\pi)^2}\int\frac{d^2\boldsymbol{\ell}'}{(2\pi)^2} w^{\phi}_{\boldsymbol{L},\boldsymbol{\ell}} w^{\phi}_{-\boldsymbol{L},\boldsymbol{\ell}'} \times [\overline{\boldsymbol{C}}^{\rm EE}_{\boldsymbol{\ell},\boldsymbol{\ell}'}\overline{\boldsymbol{B}}_{\boldsymbol{L}-\boldsymbol{\ell}}\overline{\boldsymbol{B}}_{-\boldsymbol{L}-\boldsymbol{\ell}'} + \overline{\boldsymbol{C}}^{\rm BB}_{\boldsymbol{L}-\boldsymbol{\ell},-\boldsymbol{L}-\boldsymbol{\ell}'}\overline{\boldsymbol{E}}_{\boldsymbol{\ell}}\overline{\boldsymbol{E}}_{\boldsymbol{\ell}'} - \overline{\boldsymbol{C}}^{\rm EE}_{\boldsymbol{\ell},\boldsymbol{\ell}'}\overline{\boldsymbol{C}}^{\rm BB}_{\boldsymbol{L}-\boldsymbol{\ell},-\boldsymbol{L}-\boldsymbol{\ell}'} + \overline{\boldsymbol{C}}^{\rm EB}_{\boldsymbol{\ell}',\boldsymbol{L}-\boldsymbol{\ell}}\overline{\boldsymbol{E}}_{\boldsymbol{\ell}}\overline{\boldsymbol{B}}_{-\boldsymbol{L}-\boldsymbol{\ell}'} + \overline{\boldsymbol{C}}^{\rm EB}_{\boldsymbol{\ell},-\boldsymbol{L}-\boldsymbol{\ell}'}\overline{\boldsymbol{E}}_{\boldsymbol{\ell}'}\overline{\boldsymbol{B}}_{\boldsymbol{L}-\boldsymbol{\ell}} - \overline{\boldsymbol{C}}^{\rm EB}_{\boldsymbol{\ell},-\boldsymbol{L}-\boldsymbol{\ell}'}\overline{\boldsymbol{C}}^{\rm EB}_{\boldsymbol{\ell}',\boldsymbol{L}-\boldsymbol{\ell}}]. \quad (32)$$

For example, replacing the covariance matrix with an incorrect covariance model, $\overline{\boldsymbol{C}}^{\rm EE} + \Sigma^{\rm EE}$, we obtain

$$\widehat{N}^{\phi}_{\boldsymbol{L}} = (A^{\phi}_L)^2\int\frac{d^2\boldsymbol{\ell}}{(2\pi)^2}\int\frac{d^2\boldsymbol{\ell}'}{(2\pi)^2} w^{\phi}_{\boldsymbol{L},\boldsymbol{\ell}} w^{\phi}_{-\boldsymbol{L},\boldsymbol{\ell}'} \times \Sigma^{\rm EE}_{\boldsymbol{\ell},\boldsymbol{\ell}'}(\overline{\boldsymbol{B}}_{\boldsymbol{L}-\boldsymbol{\ell}}\overline{\boldsymbol{B}}_{-\boldsymbol{L}-\boldsymbol{\ell}'} - \overline{\boldsymbol{C}}^{\rm BB}_{\boldsymbol{L}-\boldsymbol{\ell},-\boldsymbol{L}-\boldsymbol{\ell}'}) + \mathcal{O}([\Sigma^{\rm EE}]^2), \quad (33)$$

and $\langle\widehat{N}^{\phi}_{\boldsymbol{L}}\rangle$ has no contribution from $\mathcal{O}(\Sigma^{\rm EE})$.

Note that the estimators for $C^{\varpi\varpi}_L$ and $C^{\phi\varpi}_L$ are also derived in the same way (Namikawa & Takahashi 2014). The estimator for the curl-mode power spectrum is given by replacing $\widehat{\phi}_{\boldsymbol{L}}$ with $\widehat{\varpi}_{\boldsymbol{L}}$, while the disconnected bias for $C^{\phi\varpi}_L$ is estimated from

$$\widehat{N}^{\phi\varpi}_{\boldsymbol{L}} = \langle\Re[(\widehat{\phi}^{E_1,\widehat{B}}_{\boldsymbol{L}} + \widehat{\phi}^{\widehat{E},B_1}_{\boldsymbol{L}})(\widehat{\varpi}^{E_1,\widehat{B}}_{\boldsymbol{L}} + \widehat{\varpi}^{\widehat{E},B_1}_{\boldsymbol{L}})^*]\rangle_1 - \frac{1}{2}\langle\Re[(\widehat{\phi}^{E_1,B_2}_{\boldsymbol{L}} + \widehat{\phi}^{E_2,B_1}_{\boldsymbol{L}})(\widehat{\varpi}^{E_1,B_2}_{\boldsymbol{L}} + \widehat{\varpi}^{E_2,B_1}_{\boldsymbol{L}})^*]\rangle_{1,2}. \quad (34)$$

REFERENCES

Abazajian, K. N., Arnold, K., Austermann, J., et al. 2015, APh, 63, 66
Allison, R., Caucal, P., Calabrese, E., Dunkley, J., & Louis, T. 2015, PhRvD, 92, 123535
Benson, B. A., Cliche, J.-F., de Haan, T., et al. 2014, Proc. SPIE, 9153, 91531P
BICEP2 Collaboration I, 2014, PhRvL, 112, 241101
BICEP2 Collaboration II, 2014, ApJ, 792, 62
BICEP2 Collaboration III, 2015, ApJ, 814, 110
BICEP2 Collaboration IV, 2015, ApJ, 806, 206
BICEP2/*Keck Array* Collaborations V, 2015, ApJ, 811, 126
BICEP2/*Keck Array* Collaboration VI, 2015, PhRvL, 116, 031302
BICEP2/*Keck Array* Collaboration VII, 2016, ApJ, 825, 66
BICEP2 & *Planck* Collaborations 2015, PhRvL, 114, 101301
Bonvin, C., Durrer, R., & Maartens, R. 2014, PhRvL, 112, 191303
Cooray, A., Kamionkowski, M., & Caldwell, R. R. 2005, PhRvD, 71, 123527
Das, S., Sherwin, B. D., Aguirre, P., et al. 2011, PhRvL, 107, 021301
Das, S., Louis, T., Nolta, M. R., et al. 2014, JCAP, 04, 014
Dvorkin, C., & Smith, K. M. 2009, PhRvD, 79, 043003
Giannantonio, T., Fosalba, P., Cawthon, R., et al. 2015, MNRAS, 456, 3213
Hanson, D., Challinor, A., Efstathiou, G., & Bielewicz, P. 2011, PhRvD, 83, 043005
Hanson, D., Challinor, A., & Lewis, A. 2010, GReGr, 42, 2197
Hanson, D., & Lewis, A. 2009, PhRvD, 80, 063004
Hanson, D., Rocha, G., & Gorski, K. 2009, MNRAS, 400, 2169
Hanson, D., Hoover, S., Crites, A., et al. 2013, PhRvL, 111, 141301
Hirata, C. M., & Seljak, U. 2003a, PhRvD, 67, 043001
Hirata, C. M., & Seljak, U. 2003b, PhRvD, 68, 083002
Hu, W. 2001, ApJL, 557, L79
Hu, W. 2002, PhRvD, 65, 023003
Hu, W., Hedman, M., & Zaldarriaga, M. 2003, PhRvD, 67, 043004
Hu, W., & Okamoto, T. 2002, ApJ, 574, 566
Kesden, M. H., Cooray, A., & Kamionkowski, M. 2002, PhRvL, 89, 011304
Kesden, M. H., Cooray, A., & Kamionkowski, M. 2003, PhRvD, 67, 123507
Kirk, D., Omori, Y., et al. 2016, MNRAS, 459, 21
Knox, L., & Song, Y.-S. 2002, PhRvL, 89, 011303
Lee, S., Liu, G.-C., & Ng, K.-W. 2015, PhLB, 746, 406
Lewis, A. 2005, PhRvD, 71, 083008
Lewis, A., & Challinor, A. 2006, PhR, 429, 1
Lewis, A., Challinor, A., & Hanson, D. 2011, JCAP, 03, 018
LSST Dark Energy Science Collaboration, 2012, arXiv:1211.0310
Marian, L., & Bernstein, G. M. 2007, PhRvD, 76, 123009
Miller, N. J., Shimon, M., & Keating, B. G. 2008, PhRvD, 79, 063008
Namikawa, T., Hanson, D., & Takahashi, R. 2013, MNRAS, 431, 609
Namikawa, T., Saito, S., & Taruya, A. 2010, JCAP, 12, 027
Namikawa, T., & Takahashi, R. 2014, MNRAS, 438, 1507
Namikawa, T., Yamauchi, D., Sherwin, D., & Nagata, R. 2016, PhRvD, 93, 043527
Namikawa, T., Yamauchi, D., & Taruya, A. 2012, JCAP, 1201, 007

Pan, Z., & Knox, L. 2015, MNRAS, 454, 3200
Pearson, R., Sherwin, B., & Lewis, A. 2014, PhRvD, 90, 023539
Planck Collaboration, 2014a, A&A, 571, A17
Planck Collaboration, 2014b, A&A, 571, A18
Planck Collaboration, 2014c, A&A, 571, A30
Planck Collaboration, 2015, arXiv:1502.01591
POLARBEAR Collaboration, 2014a, PhRvL, 112, 131302
POLARBEAR Collaboration, 2014b, PhRvL, 113, 021301
POLARBEAR Collaboration, 2015, PhRvD, 92, 123509
Pogosian, L., & Wyman, M. 2008, PhRvD, 77, 083509
Pospelov, M., Ritz, A., & Skordis, C. 2009, PhRvL, 103, 051302
Pratten, G., & Lewis, A. 2016, arXiv:1605.05662
Regan, D., Shellard, E., & Fergusson, J. 2010, PhRvD, 82, 023520
Saga, S., Yamauchi, D., & Ichiki, K. 2015, PhRvD, 92, 063533
Seljak, U., & Hirata, C. M. 2004, PhRvD, 69, 043005
Seljak, U., & Slosar, A. 2006, PhRvD, 74, 063523
Shaw, J. R., & Lewis, A. 2010, PhRvD, 81, 043517
Sherwin, B. D., & Schmittfull, M. 2015, PhRvD, 92, 043005
Sigurdson, K., & Cooray, A. 2005, PhRvL, 95, 211303
Simard, G., Hanson, D., & Holder, G. 2015, ApJ, 807, 166
Smith, K. M., Zahn, O., & Dore, O. 2007, PhRvD, 76, 043510
Smith, K. M., Hanson, D., LoVerde, M., Hirata, C. M., & Zahn, O. 2012, JCAP, 1206, 014
Story, K. T., Hanson, D., Ade, P. A. R., et al. 2015, ApJ, 810, 50
Su, M., Yadav, A. P. S., & Zaldarriaga, M. 2009, PhRvD, 79, 123002
The Dark Energy Survey Collaboration, 2016, MNRAS, 460, 1270
The DESI Collaboration, 2013, arXiv:1308.0847
Tolan, J. E. 2014, PhD thesis, Stanford University
van Engelen, A., Keisler, R., Zahn, O., et al. 2012, ApJ, 756, 142
van Engelen, A., Sherwin, B. D., Sehgal, N., et al. 2015, ApJ, 808, 9
Wu, W. L. K., Errard, J., Dvorkin, C., et al. 2014, ApJ, 788, 138
Zaldarriaga, M., & Seljak, U. 1998, PhRvD, 58, 023003